Using UAV-based Technology to Enhance Landslide Investigation: A Case Study in Fei Ngo Shan, Kowloon

W. Hou*, J.R. Hart, R. Tsui, A. Ng & C. Cheung

GeoRisk Solutions Limited, Hong Kong

*Corresponding author
doi: https://doi.org/10.21467/proceedings.126.8

Abstract

Establishing landslide models plays a critical role in Natural Terrain Hazard Studies (NTHS). Conventional approaches adopted by NTHS practitioners may be subject to temporal and spatial limitations. In particular, landslide volume estimations are prone to inaccuracies using conventional approaches including direct, field-based measurements due to time and access constraints. With the rapid advancement of unmanned aerial vehicle (UAV) and 'Structure from Motion' (SfM) technologies in recent years, digital methods are being developed to provide useful and practical tools, which can be applied quickly, to enhance the results of landslide mapping. In this paper, we present a natural terrain landslide case study from a cluster of landslides, which were probably triggered by an intense short-duration rainstorm on 6 June 2020 at Fei Ngo Shan, Kowloon. Following initial landslide inspections to establish a preliminary engineering geological model for the failure, a digital approach was applied using a UAV-SfM derived point cloud to construct a 3D spatial model of the scar. A key objective of the 'drone survey' was to provide an alternative and accurate method of landslide volume measurement. The results demonstrate that a combination of conventional mapping and digital modeling techniques using UAV-captured data, results in enhanced landslide models for investigations and NTHS.

Keywords: UAV, Landslide investigation, Natural Terrain

1 Introduction

1.1 Background

The presence of a 'fresh' natural terrain landslide, i.e. a recently occurred landslide which is relatively clear of vegetation cover, is of great value to natural terrain hazard study (NTHS) practitioners, as it offers a unique opportunity to investigate, first-hand, active natural terrain failure mechanisms within a study catchment. Investigations on landslide failure scale, materials and mechanisms provide critical data for the derivation and discussion of future landslide design events and, therefore, for the subsequent development of appropriate hazard mitigation strategies. Conventional approaches to the investigation of natural terrain landslides involve direct field-based measurements (assuming safe field access), typically using hand-held tape measures, to estimate and record the extent and dimensions of the landslide scar. However, this approach has a number of significant limitations given the time and difficulties often involved in reaching the scar, together with the inherent challenges associated with the physical methods of accurately mapping the scar shape. In addition, there are further limitations with the use of the standard formula $W_r \times L_r \times D_r \times \pi/6$ (IAEG, 1990), which is commonly adopted to calculate landslide source area volume. This formula, whilst extremely useful to estimate a range of possible landslide volumes, assumes a rotational sliding mechanism and is

Proceedings DOI: 10.21467/proceedings.126; Series: AIJR Proceedings; ISSN: 2582-3922; ISBN: 978-81-954993-7-3

based on the assumption of ellipsoidal landslide geometry, assumptions which may not readily apply to natural terrain landslides commonly occurring in Hong Kong.

With the rapid advancement in unmanned aerial vehicle (UAV) technology in recent years, UAV-based photogrammetry has become a useful tool for landslide investigation. In conjunction with the previous territory-wide LiDAR survey in Hong Kong, this technology-driven approach can overcome a number of temporal and spatial limitations in conventional landslide investigations and provide accurate, relatively quick and cost-effective, 3D landslide models. In this paper, we present a case study from an investigation of recent landslides that occurred in June 2020 at Fei Ngo Shan, Kowloon, using digital measures, i.e. UAV-based photogrammetry, point cloud, GIS, LiDAR etc., to enhance the results of landslide field mapping.

1.2 Study Area

The study area is located at the mid- to lower portion of southeast-facing hillside slopes below Fei Ngo Shan (Kowloon Peak) (Figure 1). Within the study area, a cluster of eight landslides, named as RC15-RC22, were observed in June 2020 (Figure 2). The landslides were most likely triggered by a heavy rainstorm between 2:00 am and 6:00 am on 6 June 2020 (based on detailed rainfall analysis). A Black Rainstorm Warning signal was issued on the same day by the Hong Kong Observatory due to incessant downpours across the territory at that time.

A preliminary UAV survey and field mapping were carried out in August 2020. According to the preliminary field work and interpretation on UAV-captured aerial photos, the landslides were debris avalanches with source widths and lengths ranging from 5 m to 13 m, source depths (perpendicular to the assumed original ground surface profile) ranging from 1 m to 2.5 m, and debris trail lengths ranging from 24 m to 70 m. The estimated source volumes range from 13 m^3 to 144 m^3. The landslides typically involved the failure of bouldery colluvium overlying tuff saprolite (i.e. predominantly completely decomposed tuff) and locally moderately decomposed coarse ash tuff. Details are provided in Table 1. Among these eight landslides, the largest, RC15, was selected for detailed field mapping and further analysis.

Table 1. Inventory of 2020 landslide cluster

Landslide No.	Type*	Width of source (m)	Length of source (m)	Depth of source (m)	Estimated source volume (m^3)**	Length of debris trail (m)***	Main materials involved in the failure****
RC15	DA	11	10	2.5	144	70	Colluvium
RC16	DA	12	13	1.5	81.6	55	Bouldery colluvium overlying CDT
RC17	DA	8.5	10.5	1.5	70	40	Colluvium
RC18	DA	5	5	1	13.1	10	-
RC19	DA	7.5	7	1.5	41.2	32	-
RC20	DA	13	8.5	1	57.8	24	Thin colluvium overlying CDT (& HDT)
RC21	DA	5	6	1	15.7	35	-
RC22	DA	7.5	10.5	1.5	61.8	70	Thin colluvium overlying HDT & MDT

* DA refers to Debris avalanche; ** Source volume is based on W × L × D × π/6 (IAEG, 1990); dimensions of landslide source (i.e. W, L & D) of RC15 are from field mapping, and for others they are from UAV photograph based API; *** Length of debris trial of RC15 is from field mapping, and for others they are from UAV photograph based API; **** CDT, HDT and MDT refer to completely (C), highly (H) and moderately (M) decomposed (D), coarse ash tuff (T)

Proceedings DOI: 10.21467/proceedings.126
ISBN: 978-81-954993-7-3

Series: AIJR Proceedings
ISSN: 2582-3922

1.3 Published Geology

According to the 1:20,000-scale geological map of Hong Kong (Sheet 11, Edition II) (GEO, 2012), the study area is underlain by the Mount Davis Formation, forming part of the Lower Cretaceous Repulse Bay Volcanic Group (Figure 3).

The Mount Davis Formation is at least 500 m thick and comprises variably lapilli-bearing, coarse ash crystal tuff, with some eutaxite and sandstone beds at the type locality (GEO, 2000). In eastern Kowloon, this formation is approximately 950 m thick and includes several thick eutaxite units (GEO, 2000).

A band of eutaxitic crystal-bearing fine ash vitric tuff and a thin band of quartzphyric rhyolite dykes are present at the crest of the hillside above the study area, and these are aligned sub-parallel to the strike of the volcanic strata. An approximately N-S striking layer of tuff breccia and pyroclastic breccia is present on the slopes to the northeast of the study area. Granite of the Mount Butler Formation is present at approximately 250 m to the south of the study area.

A NE-SW aligned fault is inferred to the east of the study area. Major regional faults are mostly orientated NE-SW and NW-SE, and occasionally E-W. However, there are no faults indicated within the study area. The study area comprises an area of undifferentiated colluvium present along the valley floor.

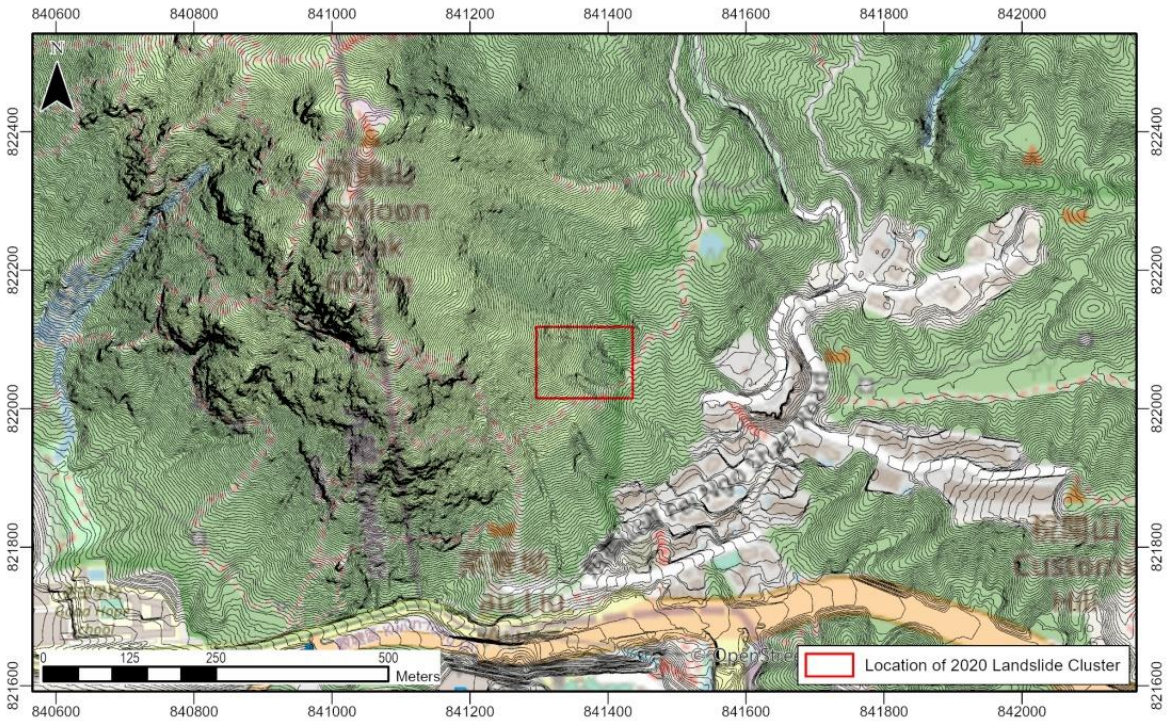

Figure 1: Location of the recent landslide cluster (June 2020). Basemap is taken from Esri OpenStreetMap (OSM contributors, 2015); contour is taken from the 2010 LiDAR survey of Hong Kong (AAM Pty Ltd, 2012).

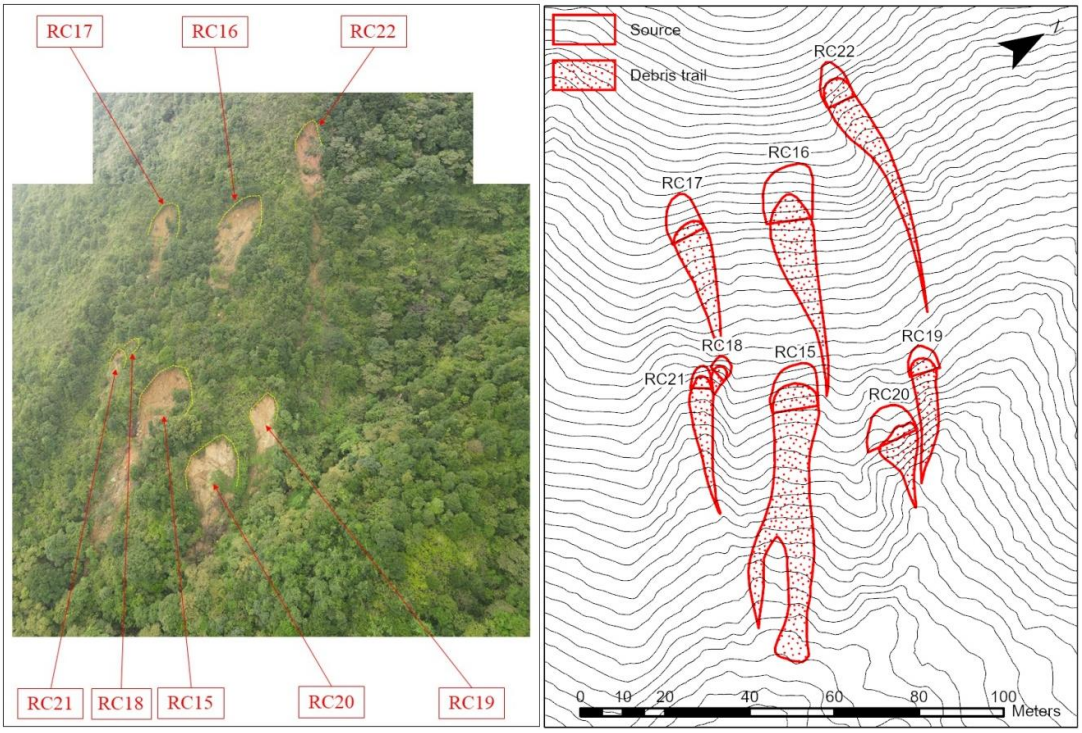

Figure 2: Overview of the recent landslide cluster (June 2020). Left: UAV photograph showing an overview of the landslide cluster. Right: a plan showing the source area and debris trail of each landslide in the cluster. Note: basemap contours are taken from the 2010 LiDAR survey of Hong Kong (AAM Pty Ltd, 2012).

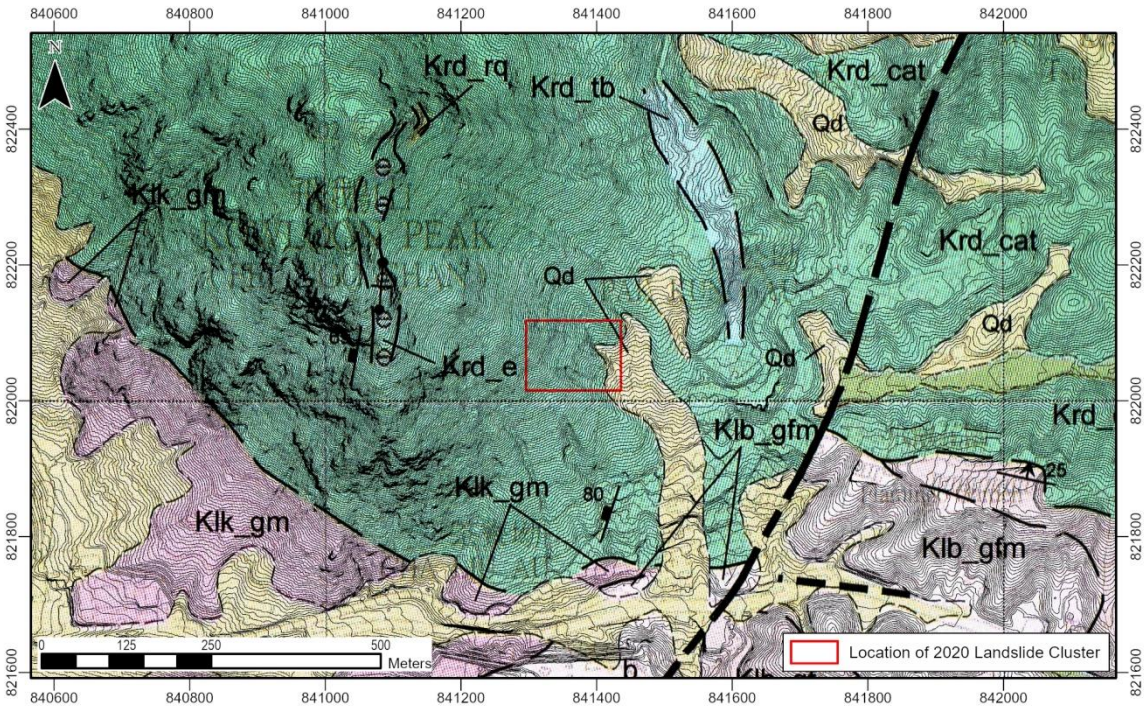

Legend - Superficial deposits: Qd Pleistocene & Holocene undifferentiated colluvium (silt, sand and gravel with boulders); Solid geology: Klb_gfm Fine to medium-grained granite (Mount Butler Granite) Klk_gm Medium-grained biotite granite (Kowloon Granite) Krd_cat Coarse ash crystal tuff (Mount Davis Fm) Krd_e Eutaxitic crystal-bearing fine ash vitric tuff (Mount Davis Fm) Krd_tb Tuff breccia & pyroclastic breccia (Mount Davis Fm) Krd_rq Quartzphyric rhyolite, mainly dykes (Mount Davis Fm); Geological lines: — — Approximate fault — — Approximate contact; Structural symbols: 22 Inclined intrusive contact 60 Inclined joint.

Figure 3: Geological map. Extracted from GEO (2012) and overlaid with 2010 LiDAR-derived contours (AAM Pty Ltd, 2012).

Proceedings DOI: 10.21467/proceedings.126
ISBN: 978-81-954993-7-3

Series: AIJR Proceedings
ISSN: 2582-3922

1.4 Geomorphology and Hydrology

Along with detailed aerial photograph interpretation (API), digital analysis of the 2010 LiDAR data (AAM Pty Ltd, 2012) was carried out to identify and map prominent geomorphological features within and in close proximity of the study area. A Digital Elevation Model (DEM) of 0.5 m resolution for the study area and adjacent terrain was generated from the LiDAR data. This LiDAR-derived DEM is used to: (1) establish a digital 3D ground model; (2) investigate topographic, hydrological and geomorphological features; and, (3) assist in determining geomorphological units by automated landform classification as part of the development of a geomorphological model for the study area.

According to the slope angle map derived from the DEM (Figure 4), the study area is characterised by three sub-horizontal bands of steeply (i.e. >45°) slopes at 350 mPD to 360 mPD (Upper band), 330 mPD to 340 mPD (middle band) and 300 mPD to 310 mPD (lower band). The upper band is the location of the source area of RC22, the middle band is the location of the source areas of RC16 and RC17, and the lower band is the location of the source areas of RC15 and RC18 to RC21. Other slopes in the vicinity are moderately inclined (i.e. 25° to 35°) to gently inclined (i.e. 15° to 25°). Flatter slopes (i.e. <15°) are present locally along the valley floor below.

The valley floor at the study site is shaped by both ephemeral and perennial streams. A stream network was generated from the DEM-based hydrological modeling (using various ArcGIS tools, e.g. flow direction, flow accumulation, stream order etc.) and is shown in Figures 4 and 5. The main streamcourse at the study site had flowing water during the entire observation period of May to December 2020 although water levels were observed to be minimal in May (i.e. at the start of the 'wet' season) and in December (i.e. within the 'dry' season). More significant stream flows were observed in August to September (i.e. within the 'wet' season). However, the subsidiary streams across the areas covered by debris from RC15 and RC21 (Figures 4 & 5) were dry during the observational period. This indicates the transient nature of surface water runoff after rainstorms. Nonetheless, these ephemeral streams provide channels for post-failure erosion of landslide scars.

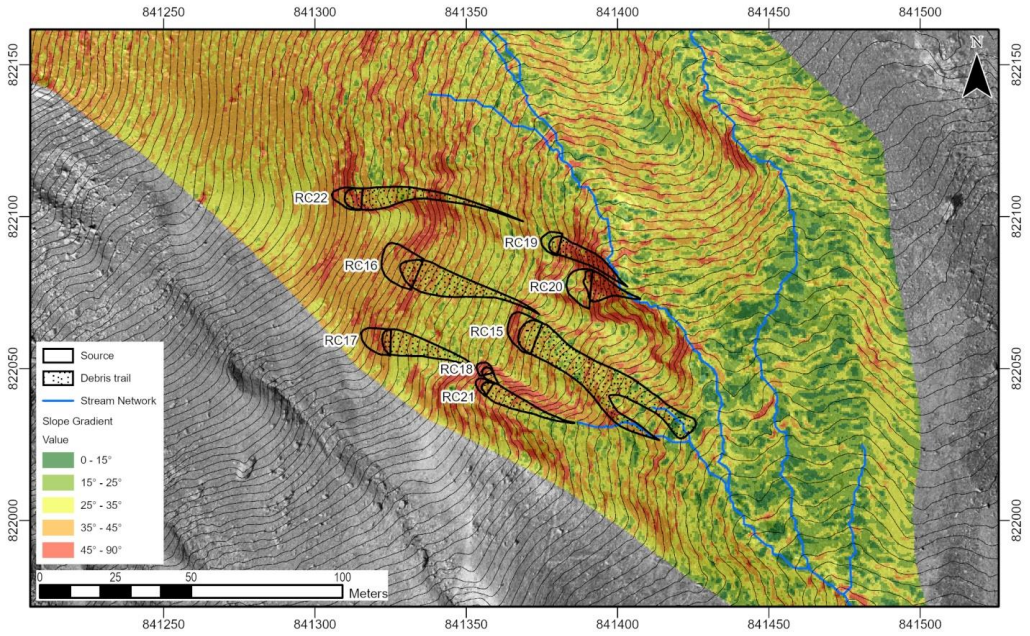

Figure 4: Slope angle map of the study area and its adjacent area and overlaid with an ortho-rectified 1963 aerial photo

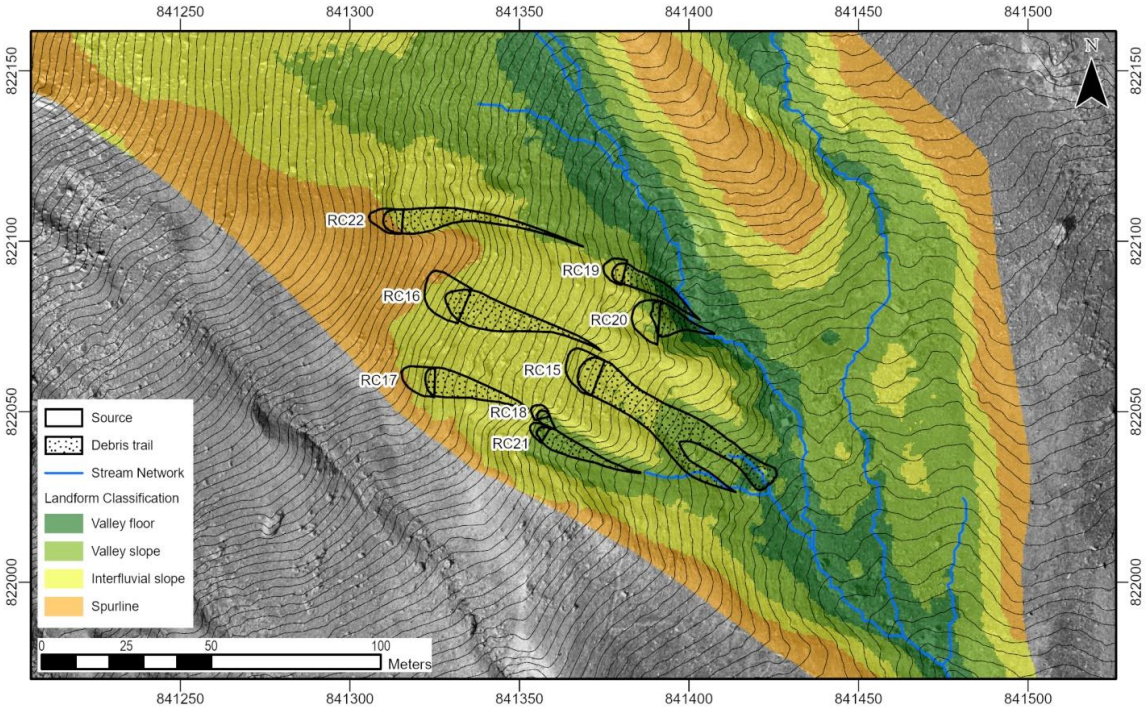

Figure 5: Automated landform classification for the study area and its adjacent area and overlaid with an ortho-rectified 1963 aerial photo

An automated approach for landform classification is applied on the LiDAR-derived DEM concerning two parameters. One parameter is the Topographic Position Index (TPI), which considers the difference between each DEM pixel and the mean elevation of its surrounding pixels (Jenness, 2006). The other parameter is the ground roughness, which considers the deviation of each DEM pixel from the mean elevation. Detailed methodology is described by De Reu et al. (2013). According to the automated landform classification (Figure 5), four geomorphological units can be determined in and adjacent to the study area. These units are valley floor, valley slope, interfluvial slope and spurline. The landform classification model shows that the source areas of RC16, RC17 and RC22 are located at the boundary between spurline and interfluvial slope. Source areas of RC18, RC19, RC20 and RC21 are located at the boundary between interfluvial slope and valley slope. RC15 occurred within the interfluvial slope.

2 Landslide Mapping

2.1 Field mapping of RC15

2.1.1 General

Detailed field mapping of RC15 (i.e. the largest landslide within the cluster) was carried out in mid-late 2020. Field photographs illustrating the key observations are presented in Figure 6. Mapping results including a plan and three section profiles are presented in Figure 7.

2.1.2 Main Scarp

The main scarp was up to 4 m high in the central portion and was steeply inclined at 80° (Figure 7 c). Bouldery colluvium was exposed in the main scarp. The colluvium was composed of stiff, orangeish brown, slightly clayey sandy silt with many cobbles and boulders. A soil pipe of approximately 0.7 m diameter and > 0.8 m long was present at the base of the main scarp (Figure 6 b). The soil pipe was

Proceedings DOI: 10.21467/proceedings.126
ISBN: 978-81-954993-7-3

Series: AIJR Proceedings
ISSN: 2582-3922

dry, approximately horizontal and partly infilled with cobbles. A 1.5 m high and 0.2-0.3 m wide tension crack was present at the lower end of the south flank of the main scarp (Figure 6 c).

2.1.3 Source Area (CH0m to CH10m)

The source area of RC15 was approximately 11 m wide, 10 m long and 2.5 m deep with an estimated source volume of 144 m^3 (Table 1, Figure 6 a & Figure 7 b). Material exposed on the surface of rupture was similar to that on the main scarp, i.e. bouldery colluvium. The upper portion of the surface of rupture is moderately steeply inclined at 45°, becoming more gently inclined at approximately 20° in the lower portion (Figure 7 c).

The surface of rupture was covered intermittently by displaced boulders and debris rafts with some relatively intact topsoil and vegetation (Figure 6 d). Large boulders predominantly rested on gently inclined slopes at the lower part of the surface of rupture. Bouldery landslide debris was locally clast-supported and voided, probably due to post-failure erosion of finer grained materials. A thin layer of finer grained landslide debris was also present on the lower part of the surface of rupture.

2.1.4 Debris Trail

Below the source area the debris trail width reduced slightly to 9 m to 10 m wide with slopes inclined at 20° to 45°. The landslide debris was thin (< 0.2 m) overlying colluvial topsoil (Figure 6 e), which probably represents the top of the older, relict, landslide debris. Lobe-shaped debris deposits were present locally and up to 0.6 m thick. The estimated volume of the debris deposited in the upper 35 m long section of the trail is approximately 50 m^3.

The debris trail bifurcated at approximately 35 m distance from the main scarp (Figure 6 f; Figure 7 a), forming two separate trails, i.e. a major trail (Figure 7 c) and a minor trail (Figure 7 d). The width of the major trail reduced to approximately 5 m.

An erosion gully was present along the major trail exposing pre-existing colluvial top soil. Landslide debris within the gully was approximately 0.1 m thick. Debris levees of approximately 0.6 m thick and 0.5 m wide were present along and above the two sides of the gully (Figure 6 g), indicating significant post-failure erosion, which had probably removed a significant amount of debris from this part of the trail.

The toe of the landslide debris was present at approximately 70 m distance along the major debris trail, with a lobe-shaped debris deposit resting on top of a man-made concrete platform (Figure 6 h).

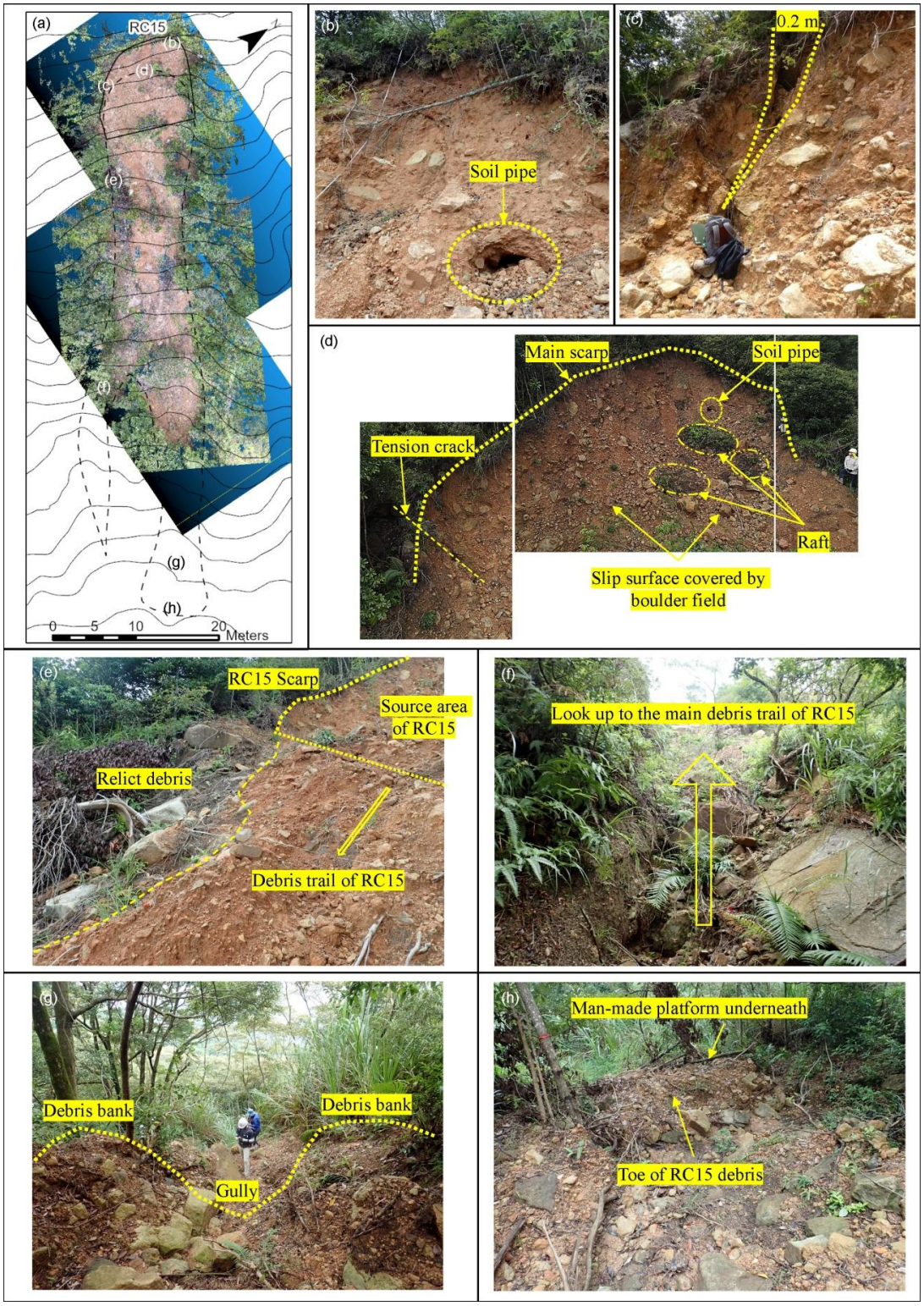

Figure 6: Photographs of RC15. (a) a plan with 2010 LiDAR contour and point cloud image showing the extent of RC15 and the locations of (b) to (h); point cloud image for the lower portion of RC15 was not available due to dense vegetation coverage; (b) soil pipe at the main scarp, approximately 0.7 m across and > 0.8 m deep; (c) minor scarp with tension crack at the south portion of main scarp, approximately 1.5 m high and up to 0.2 m wide at its widest portion near the ground surface; (d) main scarp, approximately 4 m high, inclined at 80°, with the presence of rafts and boulders below; (e) older, relict, debris below recent debris of RC15; (f) bifurcated debris trail; (g) post-failure erosion with the presence of debris banks (levees) and an incised gully within the debris; (h) debris deposited on a man-made platform at the toe.

Proceedings DOI: 10.21467/proceedings.126
ISBN: 978-81-954993-7-3

Series: AIJR Proceedings
ISSN: 2582-3922

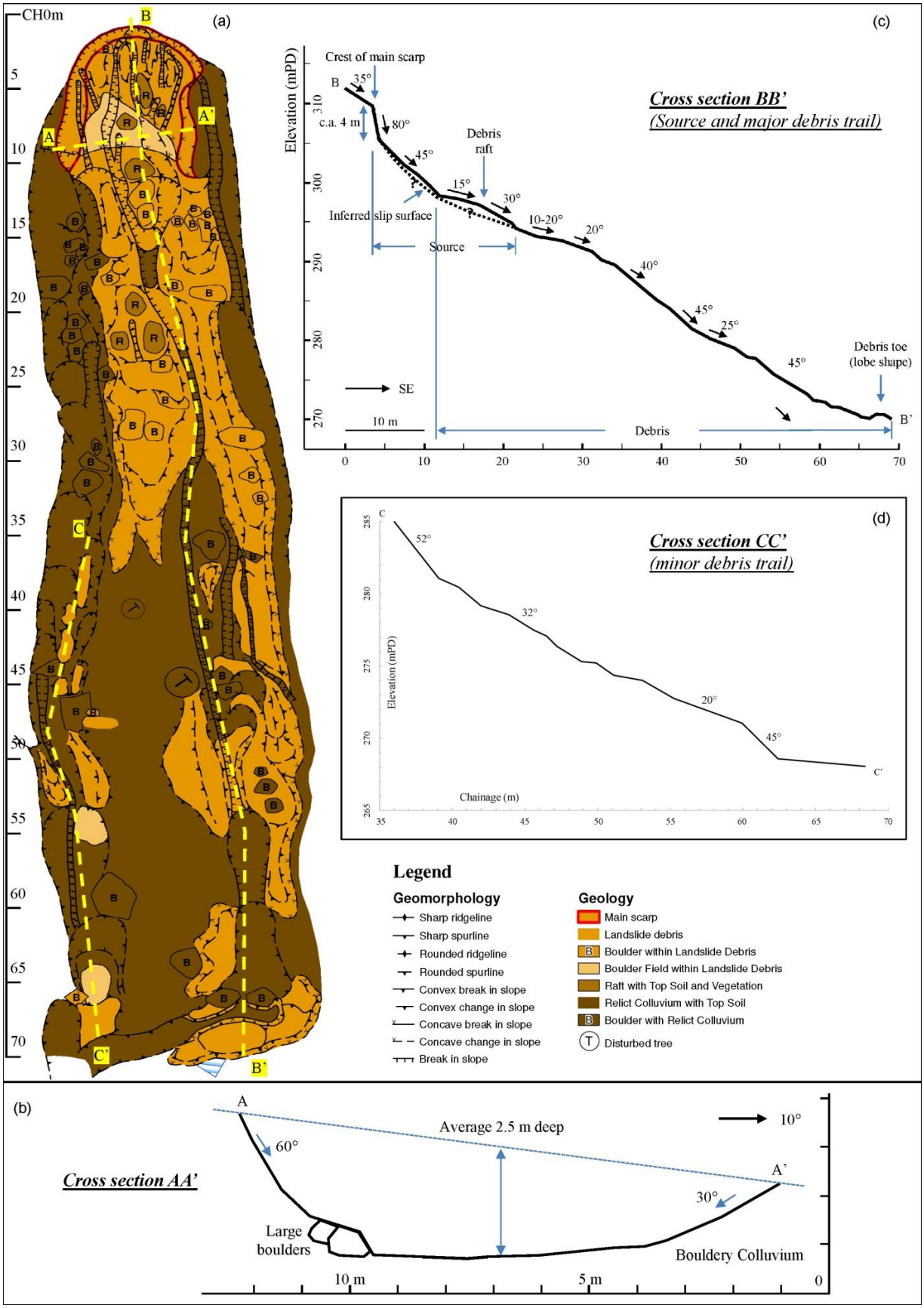

Figure 7: Field mapping of RC15. (a) mapping proforma showing the geomorphology and material of RC15; (b) cross section AA' at source area; (c) cross section BB' from crest to debris toe; (d) cross section CC' of the split debris trail.

The minor trail followed an existing drainage depression sub-parallel to the major trail. Small amounts of debris were present sporadically along the minor trail, overlying older, relict, landslide debris (Figure 7 a). The slopes in this section varied from 10° to 52° (Figure 7 c & d). The overall average slope gradient through this section was 35°. The estimated volume of debris deposited in this section is approximately 45 m^3.

2.1.5 Summary

The mapped landslide (i.e. RC15) most likely involved a debris slide in relatively thick bouldery colluvium, which transformed into a debris avalanche. The landslide debris was partially confined within an existing topographic depression, and bifurcated at 35m distance, forming two separate trails. These debris trials were confined within existing drainage depressions which have been previously affected by relict and recent landslides. Both the source area and the overall debris trail had similar widths.

According to a conventional calculation (refer to Table 1), the estimated source volume is 144 m^3. The estimated volume of the debris which was mapped along the debris trails is 95 m^3. The difference between these volumes suggests that 49 m^3 of debris (i.e. 34% of the source volume) had been removed by post-landslide erosion prior to mapping.

2.2 Photogrammetry Model of RC15

2.2.1 Methodology

In order to construct a landslide 3D model, a digital method using a UAV-based Structure from Motion (SfM) photogrammetry was applied. Using this method, a high resolution point cloud and a high accuracy DEM for the study feature, i.e. RC15, were constructed. Some researchers have demonstrated that DEMs acquired via UAV-SfM technology are comparable with those acquired via Terrestrial Laser Scanning (Tsunetaka et al., 2020), and in recent years, this method has been used in some landslide studies (Fernández et al., 2017; Cahyono and Zayd, 2018). Relevant digital tools used in this study are summarised in Table 2.

Under the current study, the point cloud for RC15 was constructed using the software Agisoft Metashape Professional (Agisoft, 2020), which generated a point cloud with accurate longitude and latitude coordinates (i.e. x and y values). However, the accuracy of the z value (i.e. elevation) of each point is limited by our UAV equipment and the relevant aerial photos. Therefore, the z value must be adjusted before calculating the landslide source volume. The adjustment of the z value in this study was carried out in ArcMap at a later stage, i.e. after point cloud data cleansing. Methods for data cleansing and z value adjustment are elaborated in the following paragraphs. It should be noted that a 3D georeferencing for all x, y and z values might be required if the Agisoft Metashape Standard version or other equivalent software is used. In this case, at least four ground control points covering the area of the study feature would be required. These can be either study-specific topographic survey points (often not available) or easily recognizable, pre-existing landmarks. For the latter method, establishing a regional model covering a larger area for georeferencing is probably needed.

Proceedings DOI: 10.21467/proceedings.126
ISBN: 978-81-954993-7-3

Series: AIJR Proceedings
ISSN: 2582-3922

Table 2. Digital tools used in this study

Digital tools	Objective / product	Notes
UAV equipped with a camera	Systematically take aerial photos for building the 3D model of the study feature RC15.	DJI Mavic Air 2 was used.
Agisoft Pro*	Produce the point cloud.	Low quality cloud was used and was sufficient for this study.
CloudCompare	Carry out point cloud data cleansing and georeferencing*.	Vegetation was removed using ERGBVEI, density and SOR.
ArcGIS	Produce DEM from the point cloud, and carry out other relevant analysis, e.g. section profiles, source volume calculation, 3D presentation etc.	Useful tools include Las to TIN, interpolate shape, raster calculator, raster to point etc.
Python	Handle large dataset calculation, particularly for testing point cloud data cleansing scalars.	Or other preferred programming language.

* Agisoft Pro version produces correct x y coordinates and incorrect z coordinate (if standard version is used, extra georeferencing of the x y values is required); adjusting z value in this study was carried out in ArcGIS.

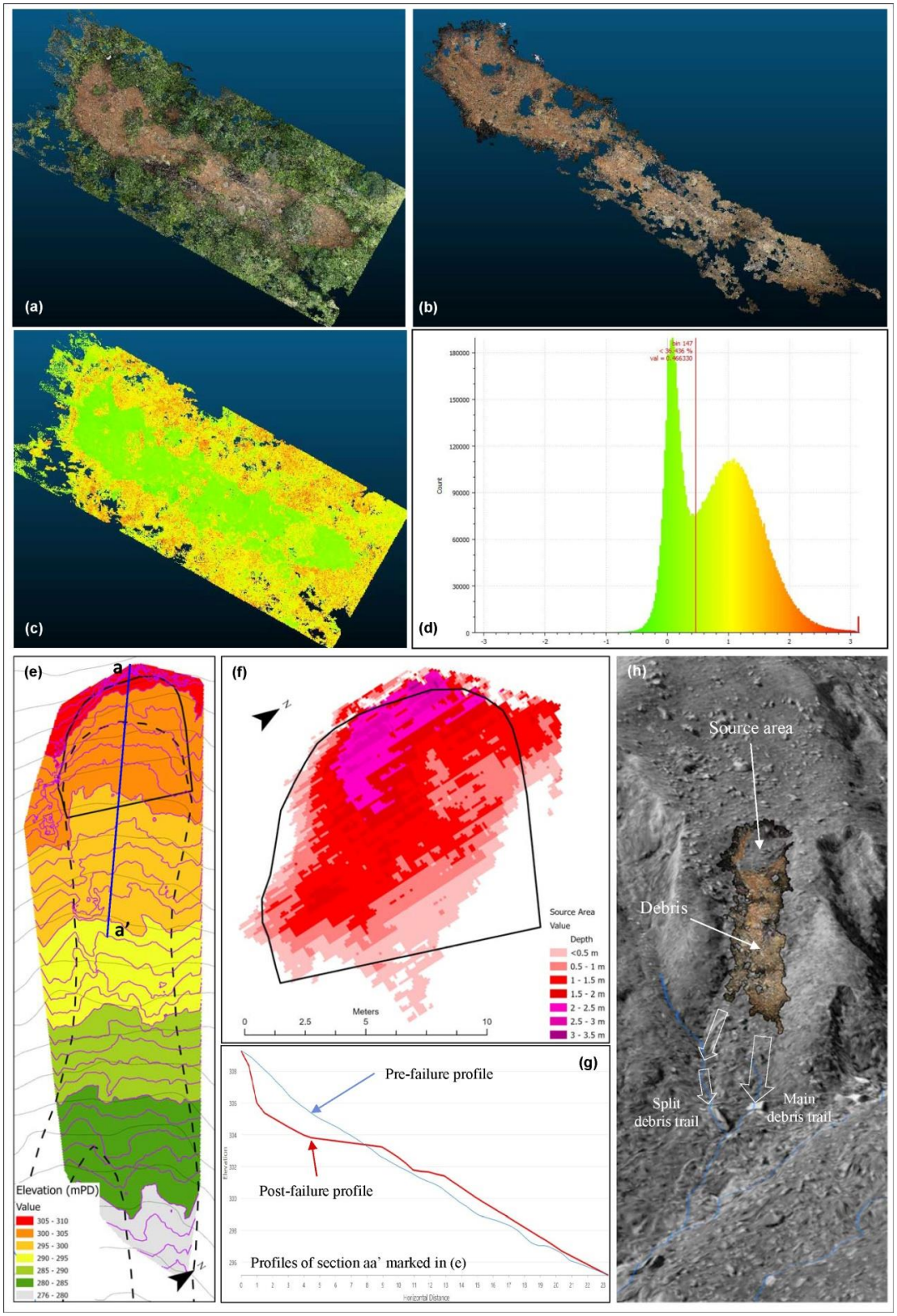

Figure 8: Photogrammetry model of RC15. (a) point cloud before data cleansing; (b) point cloud after data cleansing using firstly Enhanced RGB Vegetation Index (ERGBVI) scalar, secondly Volume Density scalar, and finally Statistical Outlier Removal tool; (c) visualisation of applying ERGBVI; (d) bimodal distribution histogram of ERGBVI showing well differentiated features (i.e. ground and vegetation); (e) DEM derived from processed point cloud showing 1 m interval post-failure contour; (f) calculation of source volume from the difference of post- and pre-failure DEMs; (g) post- and pre-failure profiles of section aa' as marked in (e); (h) 3D view of RC15 overlay 1963 aerial photograph.

Proceedings DOI: 10.21467/proceedings.126
ISBN: 978-81-954993-7-3

Series: AIJR Proceedings
ISSN: 2582-3922

The initial point cloud of RC15 generated by Agisoft Meashape comprises a high amount of vegetation signals (Figure 8 a), which must be removed before producing the DEM (Figure 8 b). In this study, the data cleansing process was carried out mainly using the software CloudCompare (2015) in the following steps. Firstly, an RGB index was calculated for all points in order to effectively classify ground features. A number of RGB-based indices have been developed by previous researchers for different purposes (Lussem et al., 2018; Wan et al., 2018; Sancho-Adamson et al., 2019). For the purpose of this study, an appropriate index was needed to effectively classify the exposed landslide scar (i.e. yellowish soil and boulders) and vegetation (greenish trees, bushes and grass). Our adopted index is the Enhanced RGB Vegetation Index (ERGBVI) introduced by Themistocleous (2019). The calculation of ERGBVI is through equation (1).

$$ERGBVI = \pi * (R_G^2 - (R_R * R_B)) / (R_G^2 + (R_R * R_B)) \quad (1)$$

where R_G = Green, R_R = Red and R_B = Blue.

The ERGBVI was then used as a scalar field in CloudCompare to filter out the vegetation. The histogram of the ERGBVI shows a bimodal pattern indicating a satisfactory result in classifying exposed ground and vegetation (Figure 8 c & d).

After applying ERGBVI index scalar filter, a substantial amount of the vegetation signals was removed. The remnant vegetation signals became evidently sparse such that they could be removed by the density scalar in CloudCompare. The final remnant vegetation signals were extremely low in amount and were removed using the Statistical Outlier Removal (SOR) tool.

The cleaned point cloud was then processed to generate a DEM of 0.1 m resolution in ArcMap (Figure 8 e). The generation of this DEM underwent two steps. Firstly, due to the incorrect z value (refer to the second paragraph of this section) of the point cloud, the initial DEM generated directly from the point cloud data was bearing incorrect elevation values. Here we call it fake-DEM. In this fake-DEM, landslide crown can be easily identified based on the steep slopes of the landslide scarp. Given that the elevation of the landslide crown is considered unchanged compared to the pre-failure ground profile, an adjusting parameter, z', can be derived by comparing the fake-DEM and the pre-failure ground profile (i.e. the 2010 LiDAR-derived DEM) at the landslide crown area. Each pixel of the fake-DEM was then added by z' to generate the final (i.e. the correct) DEM. In brief, these two steps used the landslide crown as the georeferencing area to adjust the z value.

The pre-failure DEM, i.e. derived from 2010 LiDAR, and the post-failure DEM, i.e. derived from the cleaned point cloud with the z value adjustment, were then used for calculating the failure volume (Figure 8 f & g) and for 3D visualisation (Figure 8 h).

2.2.2 Source Volume of RC15

To validate the reliability of the RC15 model, two steps were taken. Firstly, 1 m interval contours were generated for RC15 using the point cloud derived DEM (Figure 8 e) and the result shows the typical landslide depression contour pattern. Secondly, the RC15 model was embedded in the 2010 LiDAR-derived DEM with the 1963 aerial photo overlay (Figure 8 h) with the result indicating a very close fit. After the validation, the failure volume of RC15 was calculated by comparing the pre-failure and post-

failure ground profiles. The calculation process was carried out in ArcMap (Figure 8 f). The source volume of RC15 calculated by this method is 115 m^3.

2.2.3 Summary

The final result shows that construction of a 3D model for the 'fresh' landslide with UAV and SfM technology is feasible and practical. The 3D model also provides more accurate scarp and debris morphology as compared to conventional field mapping. The source volume of RC15 calculated based on the pre-failure and post-failure 3D models is slightly smaller than that calculated based on field-based measurements under the conventional approach. This smaller volume is considered more reliable given that RC15 is located within an existing depression. However, this volume may have slightly underestimated the true volume given that the calculated volume was not adjusted to take account of a small amount of debris present locally on the surface of rupture.

3 Conclusions and Future Uses

The case study shows that this UAV-based, digital method is a useful and practical tool to assist engineering geologists in natural terrain landslide investigations. It produces time-efficient and cost-effective spatial model for landslides, and provide more accurate data on failure scale, such as source area dimensions and failure volume. Our case study also shows that the conventional field mapping produces an engineering geological/ geomorphological model to serve a discussion of the mechanism, aftermath and possible pattern of landslides. A combination of these methods is able to provide a more comprehensive portrait for landslide events.

In addition to the successful practice, we also suggest some practices for future improvement. Firstly, it is noticed that our 3D model does not cover the lower part of RC15 due to dense vegetation. Therefore, either the handheld laser scanner or the LiDAR sensor mounted on a UAV (Huang et al., 2019; Pfeiffer et al., 2019) could be used to fill this gap. Secondly, with the advent of new territory-wide LiDAR survey (2020) in Hong Kong, and the possible DEMs derived from historical aerial photographs (Deane et al., 2020), e.g. 1963 photos in Hong Kong (our unpublished data), multi-temporal terrain models could be used to detect terrain changes and to provide valued backgrounds for landslide studies.

4 Acknowledgements

We would like to thank Ms Yan Au Yeng in assistance of the field mapping, and Mr. Jaime Anselmo Jr. Glemao for assistance in the GIS digitization of field notes. The 2010 LiDAR survey data has been used with the consent of the Geotechnical Engineering Office of the Civil Engineering and Development Department, of the Government of the Hong Kong SAR.

References

[1] AAM Pty Ltd 2012. *Territory-Wide Airborne Light Detection and Ranging (LiDAR) Survey*. The Government of the Hong Kong Special Administration Region, Civil Engineering and Development Department (Contract No. GE/2008/28), 14 p.

[2] Agisoft, L. L. C. 2020. Agisoft metashape user manual, Professional edition, Version 1.6. *Agisoft LLC, St. Petersburg, Russia, from https://www.agisoft.com/pdf/metashape-pro_1_6_en.pdf, accessed March, 2021*.

[3] Cahyono, A. B., & Zayd, R. A. March 2018. Rapid mapping of landslide disaster using UAV-photogrammetry. In *Journal of Physics: Conference Series*. Vol. 974, No. 1, p. 012046. IOP Publishing.

[4] CloudCompare 2015. CloudCompare User Manual Version 2.6.1. *From http://www.cloudcompare.org/doc/qCC/CloudCompare%20v2.6.1%20-%20User%20manual.pdf, accessed March, 2021*.

[5] De Reu, J., Bourgeois, J., Bats, M., Zwertvaegher, A., Gelorini, V., De Smedt, P., Chu, W., Antrop, M., De Maeyer, P., Finke, P. and Van Meirvenne, M. 2013. Application of the topographic position index to heterogeneous landscapes. *Geomorphology*, *186*, pp.39-49.

[6] Deane, E., Macciotta, R., Hendry, M., Gräpel, C., & Skirrow, R. September 2020. Historical aerial photographs and digital photogrammetry techniques to investigate the development and evolution of the Chin Coulee landslide in Alberta. In *GeoVirtual 2020*.

[7] Fernández, T., Pérez, J. L., Colomo, C., Cardenal, J., Delgado, J., Palenzuela, J. A., Irigaray, C. & Chacón, J. 2017. Assessment of the evolution of a landslide using digital photogrammetry and LiDAR techniques in the Alpujarras region (Granada, southeastern Spain). *Geosciences*, *7*(2), 32.

[8] Geotechnical Engineering Office (GEO) 2000. *The Pre-Quaternary Geology of Hong Kong*. Geotechnical Engineering Office, Civil Engineering and Development Department, Hong Kong Government.

[9] Geotechnical Engineering Office (GEO) 2012. *1:20,000-scale Solid & Superficial Geology. Sheet 11, Edition II, Hong Kong and Kowloon*. Geotechnical Engineering Office. Civil Engineering and Development Department, Hong Kong Government.

[10] Hung, C. L. J., Tseng, C. W., Huang, M. J., Tseng, C. M., & Chang, K. J. 2019. Multi-Temporal High-Resolution Landslide Monitoring Based on Uas Photogrammetry and Uas LIDAR Geoinformation. *International Archives of the Photogrammetry, Remote Sensing and Spatial Information Sciences*, *42*(3/W8).

[11] International Association of Engineering Geology (IAEG) Commission on Landslides 1990. Suggested Nomenclature for Landslides. *Bulletin of the International Association of Engineering Geology*, No. 41, pp. 13-16.

[12] Jenness, J. 2006. *Topographic Position Index extension for ArcView 3.x, v.1.2*. Jenness Enterprises.

[13] Lussem, U., Bolten, A., Gnyp, M. L., Jasper, J., & Bareth, G. 2018. Evaluation of RGB-based vegetation indices from UAV imagery to estimate forage yield in grassland. *Int. Arch. Photogramm. Remote Sens. Spatial Inf. Sci*, *42*(3), 1215-1219.

[14] OpenStreetMap (OSM) contributors 2015. *Retrieved from https://planet.openstreetmap.org*

[15] Pfeiffer, J., Zieher, T., Rutzinger, M., Bremer, M., & Wichmann, V. 2019. Comparison and time-series analysis of landslide displacement mapped by airborne, terrestrial and unmanned aerial vehicle based platforms. *ISPRS Annals of the Photogrammetry, Remote Sensing and Spatial Information Sciences*. Vol. IV-2/W5.

[16] Sancho-Adamson, M., Trillas, M. I., Bort, J., Fernandez-Gallego, J. A., & Romanyà, J. 2019. Use of RGB vegetation indexes in assessing early effects of Verticillium wilt of olive in asymptomatic plants in high and low fertility scenarios. *Remote Sensing*, *11*(6), 607.

[17] Themistocleous, K. June 2019. DEM modeling using RGB-based vegetation indices from UAV images. In *Seventh International Conference on Remote Sensing and Geoinformation of the Environment (RSCy2019)* (Vol. 11174, p. 111741J). International Society for Optics and Photonics.

[18] Tsunetaka, H., Hotta, N., Hayakawa, Y. S., & Imaizumi, F. 2020. Spatial accuracy assessment of unmanned aerial vehicle-based structures from motion multi-view stereo photogrammetry for geomorphic observations in initiation zones of debris flows, Ohya landslide, Japan. Progress in Earth and Planetary Science, 7, 1-14.

[19] Wan, L., Li, Y., Cen, H., Zhu, J., Yin, W., Wu, W., Zhu, H., Sun, D., Zhou, W. & He, Y. 2018. Combining UAV-based vegetation indices and image classification to estimate flower number in oilseed rape. Remote Sensing, 10(9), 1484.